How to cite: *Angew. Chem. Int. Ed.* **2022**, *61*, e202112204
International Edition: doi.org/10.1002/anie.202112204
German Edition: doi.org/10.1002/ange.202112204

Mesocrystals

Radiation Chemistry Provides Nanoscopic Insights into the Role of Intermediate Phases in CeO_2 Mesocrystal Formation

*Zhuofeng Li[+], Diana Piankova[+], Yi Yang, Yuta Kumagai, Hannes Zschiesche, Mats Jonsson, Nadezda V. Tarakina, and Inna L. Soroka**

Abstract: *The role of intermediate phases in CeO_2 mesocrystal formation from aqueous Ce^{III} solutions subjected to γ-radiation was studied. Radiolytically formed hydroxyl radicals convert soluble Ce^{III} into less soluble Ce^{IV}. Transmission electron microscopy (TEM) and X-ray diffraction studies of samples from different stages of the process allowed the identification of several stages in CeO_2 mesocrystal evolution following the oxidation to Ce^{IV}: (1) formation of hydrated Ce^{IV} hydroxides, serving as intermediates in the liquid-to-solid phase transformation; (2) CeO_2 primary particle growth inside the intermediate phase; (3) alignment of the primary particles into "pre-mesocrystals" and subsequently to mesocrystals, guided by confinement of the amorphous intermediate phase and accompanied by the formation of "mineral bridges". Further alignment of the obtained mesocrystals into supracrystals occurs upon slow drying, making it possible to form complex hierarchical architectures.*

Introduction

Ceria (CeO_2) based nanomaterials are of great importance in numerous applications such as catalyst supports,[1] catalysts,[2] materials for solar cells[3] and potential pharmacological agents[4] mainly due to the capacity of ceria to store and release oxygen. The extensive applications of ceria require materials having well-defined composition, structure and morphology. This required full control of the synthesis procedure in order to tune the properties of CeO_2 based nanomaterials. To achieve this, one needs to have a fundamental understanding of ceria formation and crystal growth processes.

Different routes to synthesize CeO_2 nanomaterials in cerium precursor solutions have been reported. These include thermal decomposition,[5] sonolysis[6] and sol-gel methods.[7] As shown in the literature, several steps in ceria nanoparticle formation from Ce^{III} can be identified: (i) oxidation of a Ce^{3+} salt by an oxidizing agent (H_2O_2, O_2, etc.); (ii) precipitation of intermediates, such as Ce^{IV}-hydroxide, and (iii) CeO_2 crystalline particle formation.[8–12] It has also been demonstrated that, depending on synthesis conditions, CeO_2 particles may form mesocrystals, highly-ordered nanoparticle superstructures, which diffract as a single crystal.[13–17] In other words, mesocrystals constitute a special case of colloidal crystals, implying 3D translational order of various nanocrystals (primary particles).[18] Formation of mesocrystals is an example of a non-classical crystallization pathway. Non-classical crystallization occurs via the formation of a sequence of metastable phases of increasing density.[19–22] Such sequential precipitation is often preferable since it requires to overcome smaller activation energy barriers as compared to the one-step crystallization route explained by Oswald ripening in the classical theory.[23,24] Although the general non-classical crystallization pathway proposed a while ago,[19,20] describes the formation of mesocrystals, empirical evidence is still required to verify the particular stages of growth (e.g. mechanism of three-dimensional mutual alignment of the nanoparticles and the role of intermediates) as well as the individual features in the formation of a specific compound. Due to several mutually influencing parameters which arise during synthesis, distinguishing the different stages of mesocrystal formation is difficult. To control the process of mesocrystal formation and perform the reaction without additional additives at elevated temperatures we fabricated CeO_2 mesocrystals by means of γ-radiation induced synthesis.

Aqueous radiation chemistry, i.e., chemical change induced upon absorption of ionizing radiation in water, has proven to be a versatile path enabling controlled manufacturing of both organic and inorganic nanomaterials.[25–35] Inorganic nanomaterials, including metals and metal oxides, are in general synthesized by reducing or oxidizing a soluble precursor to the desired oxidation state. Upon exposure to ionizing radiation, water is decomposed with the formation of

[*] Z. Li,[+] Y. Yang, M. Jonsson, I. L. Soroka
Department of Chemistry, School of Engineering Sciences in Chemistry, Biotechnology and Health, KTH Royal Institute of Technology
10044 Stockholm (Sweden)
E-mail: soroka@kth.se
D. Piankova,[+] H. Zschiesche, N. V. Tarakina
Max Planck Institute of Colloids and Interfaces
Am Mühlenberg 1, 14476 Potsdam (Germany)
Y. Kumagai
Nuclear Science and Engineering Center (Japan) Atomic Energy Agency
2–4 Shirane Shirakata, Tokai-mura, Naka-gun, Ibaraki 319-1195 (Japan)
[+] These authors contributed equally to this work.
Supporting information and the ORCID identification number(s) for the author(s) of this article can be found under: https://doi.org/10.1002/anie.202112204.

oxidants ($OH^{\bullet}$, H_2O_2, $HO_2^{\bullet}$) and reductants (e_{aq}^-, $H^{\bullet}$, H_2), some of which are very reactive. Through the addition of selective radical scavengers, the redox conditions of irradiated aqueous solutions can be controlled, and it is therefore possible to selectively induce one-electron reduction or oxidation. As the radiation chemical yields (or G-values) of all the radiolysis products are well-known,[36] it is also possible to control the radiation-induced reactions in a more quantitative way by varying the total absorbed dose and the dose rate (i.e., the radiation intensity).

In the current study, for the synthesis of CeO_2 from Ce^{III}, we utilize the hydroxyl radical since this is the only radiolytic oxidant that will oxidize Ce^{III} to Ce^{IV} at a sufficiently high rate. By saturating an aqueous solution with nitrous oxide, N_2O, we can convert the hydrated electron (e_{aq}^-) to a hydroxyl radical according to the following reaction:[37]

$$e_{aq}^- + N_2O + H_2O \rightarrow OH^{\bullet} + OH^- + N_2 \qquad k_1 = 9.1 \times 10^9\ s^{-1}\ mol^{-1}\ dm^3\ [38] \qquad (1)$$

As a result, the effective G-value for hydroxyl radicals in γ-radiolysis is doubled from 0.28 μmol J^{-1} to 0.56 μmol J^{-1}.[36] In a solution continuously exposed to γ-radiation at a constant dose rate, the concentrations of radicals will rapidly reach steady-state levels. The low and mostly constant concentration of radicals provides a stable and controllable way of converting soluble Ce^{III} salts into Ce^{IV} with a minimum of added chemicals. The steady-state concentrations of the short-lived radiolysis products can be fine-tuned simply by altering the intensity of the γ-radiation. Therefore, given the high level of process control we used aqueous γ-radiolysis to initiate the synthesis of CeO_2 mesocrystals, with the aim of experimentally resolving the different formation stages of ceria mesocrystals at the nanoscopic level.

Results and Discussion

Nanocrystalline ceria was synthesized by γ-radiation-induced oxidation of Ce^{III} to Ce^{IV} by hydroxyl radicals in aqueous solutions containing 5 mM $CeCl_3 \times 7H_2O$, according to the following reaction:[39]

$$Ce^{III} + OH^{\bullet} \rightarrow Ce^{IV} + HO^- \qquad k_1 = 3.0 \times 10^8\ s^{-1}\ mol^{-1}\ dm^3\ [38] \qquad (2)$$

To enhance the efficiency of the process, the solutions were saturated with N_2O to convert e_{aq}^- into $OH^{\bullet}$, see reaction (1). The dose rate of the γ-source is 0.125 Gy s^{-1} and the total absorbed dose is controlled by the irradiation time. To investigate the CeO_2 formation at different conversions, the total dose was varied from 0.04 kGy (5 min) to 10.8 kGy (24 h). The higher dose yields a total amount of hydroxyl radicals sufficient for the complete conversion of 5 mM Ce^{III} to Ce^{IV} in the absence of competing reactions. A sample synthesized at 29 kGy is used as a reference. After the reaction of Ce^{III} with $OH^{\bullet}$, a yellow precipitate containing CeO_2 particles is formed.

The structure and morphology of the obtained precipitate were first characterized by X-ray diffraction (XRD). The XRD patterns recorded from the precipitates obtained at total doses in the range 1.35–10.8 kGy are shown in Figure 1.

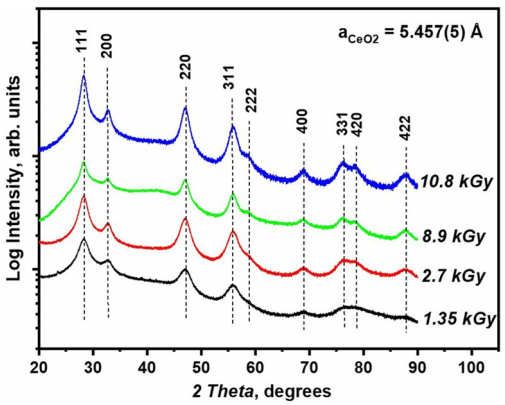

Figure 1. X-ray powder diffraction patterns of CeO_2 produced via radiolytic oxidation of Ce^{III} in aqueous solution obtained at total doses from 1.35 kGy to 10.8 kGy. The peaks are indexed in cubic CeO_2, space group $Fm\bar{3}m$. The average lattice constant and particles diameter calculated from the XRD patterns are denoted. Miller indices and the total absorption doses are labelled on the graph.

At doses lower than 1.35 kGy the amount of formed precipitate was insufficient to perform XRD measurement. As seen in the Figure, only the diffraction peaks that belong to the crystallographic planes of CeO_2 are present in the 2θ range from 20° to 90°. Analysis of the XRD patterns confirms that CeO_2 nanoparticles crystallize in a cubic lattice, space group $Fm\bar{3}m$, and can be described by the fluorite type (CaF_2) structure. Unit cell parameters calculated from recorded XRD patterns are given in Figure 1. Within the given dose interval, the lattice parameter of ceria is independent of absorbed dose. The observed unit cell parameter is larger than the lattice parameter found for bulk CeO_2 ($a = 5.412$ Å) for samples measured under ambient conditions.[40] It is well known that the lattice parameters for nanomaterials can differ from those in the bulk.[41–44] Two main models explaining the variation of lattice parameter in cerium oxide nanoparticles were proposed in the literature: (1) formation of the oxygen vacancies, and thus a change in the oxidation state of smaller nanoparticles[59] and (2) difference in the coordination of atoms in the surface and in bulk which creates surface stress; this stress increases for smaller particles.[43]

In order to get further insights into the structure and morphology of the obtained nanoparticles and to catch the early stages of the particle formation and growth, we performed ex-situ dose (time) dependent TEM investigations. Precursor solutions were exposed to gamma radiation for different times and in each case the obtained reaction mixture was drop-casted onto a TEM grid and dried directly after irradiation. The analysis of the initial precursor solution (0 kGy, Figure 2) showed the formation of amorphous drops of high contrast, which is typical for quick drying of a salt on a TEM grid. Analysis of the specimen synthesized at 0.11 kGy (15 min) revealed the presence of two morphologically

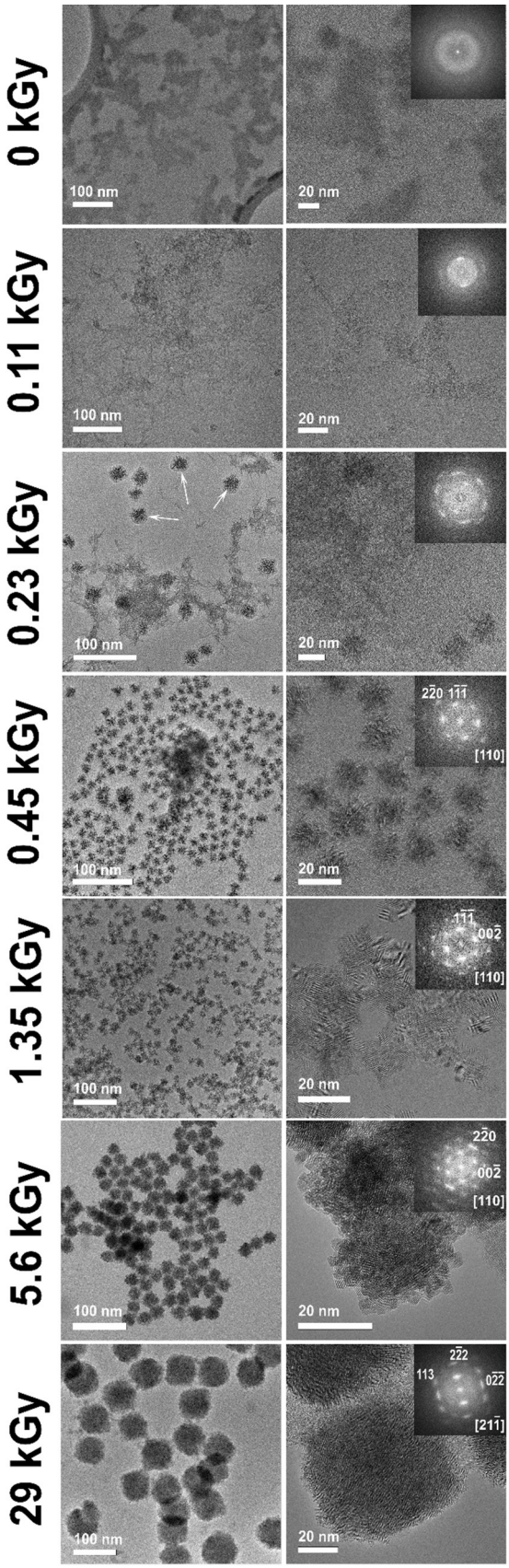

Figure 2. High Resolution Transmission Electron Microscopy, HR-TEM, images taken after $CeCl_3 \times 7H_2O$ solution was exposed to different total doses. Insets show the corresponding FFT patterns.

different phases: (1) a network of needle-like agglomerates, which appear to be amorphous and most probably form a gel in hydrated state with (2) denser areas incorporated in this network which appear to be loose nanoparticle assemblies. As shown below, the nanoparticles within the assemblies will subsequently undergo self-organization and form mesocrystals. Since there is no clear definition in the literature describing at which degree of primary particle-misalignment we can consider their assembly to be a mesocrystal we refer these assemblies as "pre-mesocrystals" until a clear single crystal-like Fast Fourier Transforms (FFT) pattern is obtained from such agglomerate.[45]

The sample synthesized at 0.23 kGy (30 min) consists of two phases as well; however, the amount of the "pre-mesocrystal" phase is higher. The "pre-mesocrystals" have a more defined shape as compared to that in the sample synthesized at 0.11 kGy, and some of them are no longer incorporated into the amorphous needle-like network but found to be surrounded by an amorphous matrix (shown with white arrows in Figure 2). The primary particles within the "pre-mesocrystals" are not yet perfectly aligned to each other, forming arcs instead of dots in the FFT patterns. Starting from 0.45 kGy only FFT patterns corresponding to the mesocrystal phase are observed. Moreover, FFT analysis reveals that the samples synthesized at higher doses than 0.45 kGy, are less disordered. The FFT patterns obtained from the images with mesocrystals can be indexed in a face-centered cubic lattice of CeO_2. As seen in Figure 2, mesocrystals increase in size and develop a more defined morphology, from a star-like/pentagonal shape in projection (sample obtained at 0.45 kGy) toward a truncated square shape in projection (at higher doses).

The non-spherical morphology of the synthesized mesocrystals is confirmed by the bi-modal size distribution obtained from HR-TEM images and illustrated in Figure 3(a). The trends for the diameter as a function of dose within the given dose-range for both mesocrystals and primary particles display similar tendencies. Sizes of both primary particles and mesocrystals increase with dose and reach a plateau, at 1.35 kGy and 2.7 kGy, respectively, see Figure 3(b). To verify if the self-assembly of particles is driven by radiation or by the residence time in the solution, additional experiments have been performed. A set of samples was irradiated at doses 1.35, 2.7, 9.0 and 10.8 kGy and were kept in solution for several days after irradiation. Thereafter, the morphology of these samples was compared to that of the samples prepared immediately after irradiation. No significant difference in primary particle size or mesocrystal size between these sets of samples was observed. We also compared the size of the primary particles of the mesocrystals obtained from Ce precursor solutions of different concentrations (Figures S1, S2 and Table S1), no significant differences in primary particle size as a function of initial Ce^{3+} concentration have been found. It is worth mentioning, that for samples synthesized at high doses ($\geq$29 kGy), the mesocrystal diameter increases; in different samples it varies between 50 and 80 nm and does not show correlation with the total dose. At the same time, the diameters of the primary particles remain unchanged even at such high doses ($\approx$3 nm).

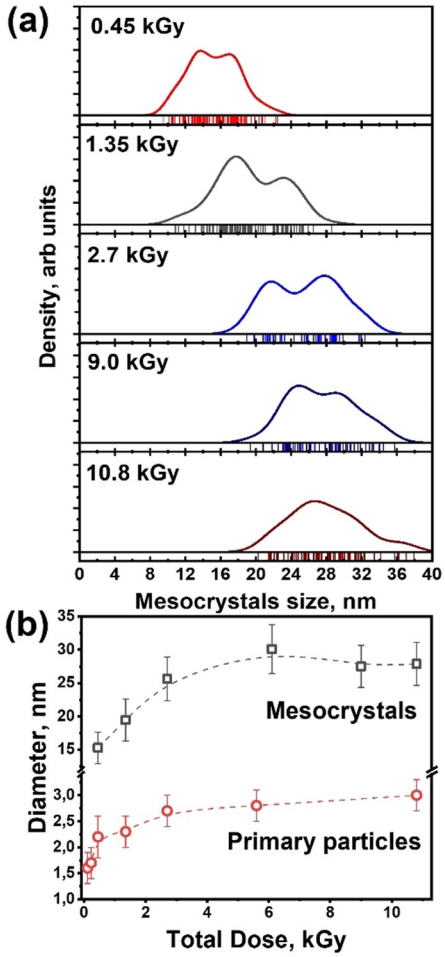

Figure 3. a) Lognormal size distributions of mesocrystals obtained at different doses. The total absorbed doses are given in the Figure; b) The average diameters of primary particles and mesocrystals calculated from HR-TEM images and plotted vs. total absorbed doses.

Further growth may happen due to the aggregation of the mesocrystals.[46]

To deepen our understanding of the early events of the process, we analyzed the electron radial distribution functions obtained from zero-loss energy filtered electron diffraction patterns (EF-eRDF). Figure 4(b) shows the evolution of the EF-eRDFs with respect to the absorbed dose. The signal starts to differ from that of the pure carbon support at doses $\geq$0.23 kGy, probably due to the low amount and the weak scattering power of the needle-like agglomerates mainly found at low doses. The samples obtained at 0.23 and 0.90 kGy demonstrate structural correlations of 20 Å and 24 Å, respectively. At these doses primary particles grow and the needle-like phase disappears. Intensity ratios of the peaks in the first and the second coordination spheres are different compared to those in the samples obtained at higher doses ($\geq$ 1.35 kGy) which can be explained by low crystallinity of "pre-mesocrystals" and/or by the presence of the amorphous needle-like phase. The samples synthesized at doses $\geq$1.35 kGy have almost the same structural correlation as the sample synthesized at 29 kGy (used as a reference CeO_2 sample); the cut-off distances of the eRDFs are 29 Å and 30 Å, respectively. Starting from the 0.23 kGy sample, all obtained EF-eRDFs can be described using the cubic CeO_2 structure, see Figure 4(a). Analysis of EF-eRDFs clearly shows that primary nanoparticles are fully formed already after 3 hours (1.35 kGy) of irradiation, which together with the TEM results indicates that at higher doses processes of oriented attachments and growth of mesocrystals are dominant.

Further details of the oriented attachment and growth of mesocrystals were clarified with an explicit analysis of HRTEM at 1.35 kGy and 5.6–6.1 kGy, see Figure 5 and Figure 6. The sample obtained after 3 hours irradiation (1.35 kGy) shows that within each mesocrystal there are regions of 5–10 nm in which primary particles are well aligned, giving almost single-crystalline FFTs (Figure 5, dashed circles). Several such regions interconnect, but in most cases, they are not yet perfectly aligned to one mesocrystal. The mesocrystals, in general, appear to form a very loose network, connecting through primary particles. Figure 5(b) shows several primary particles forming a bridge between two mesocrystals. They are all oriented along different directions with respect to the beam, however the [1−10] axis of these three neighboring particles (FFTs of which are marked with green, yellow and blue colors in Figure 5(b)) is pointing to the same direction, giving guidance to further alignment. The corresponding projections of CeO_2 unit cells are shown in Figure 5(c), highlighting the almost parallel alignment of the (1−10) planes in three neighboring particles.

Mesocrystals formed at 5.6–6.1 kGy are larger (of about 30 nm) and have much more defined shapes. They still form a network through bridges of primary particles. The pentagonal symmetries are dominant for the mesocrystals at this stage but many particles also start to have a cuboid morphology (Figure 2 and Figure 6). In general, primary particles are better aligned and the majority of the mesocrystals show single-crystalline FFT patterns, with a slight degree of misalignment of the primary particles, however in some cases different areas of the mesocrystals can have different orientations, which indicates that the process of the alignment is not yet completed at this stage.

In general, the radiolytic formation of CeO_2 from Ce^{III} in aqueous solution should proceed via the following steps: (1) oxidation of Ce^{III} to Ce^{IV} according to Reaction 2, (2) hydration and hydrolysis of Ce^{IV}, (3) aggregation of hydrated Ce^{IV}-hydroxides, forming gel and finally (4) condensation of the aggregated Ce^{IV}-hydroxides into CeO_2.[47,48] The overall reaction Scheme is depicted in Figure 7.

The latter two steps are often referred to as olation and oxolation, respectively. The hydrolysis ratio for a given metal cation is pH-dependent[49] and it is interesting to note that the solution pH changes significantly during irradiation in this case. This is illustrated in Figure 8(a).

As a result of the decreasing pH with increasing dose, Ce^{IV}-hydroxide will contain more OH^- at low doses than at higher doses.[47] In general, the solubility of metal hydroxides (and oxides) increases with decreasing pH.[50] In other words, the solubility should increase during the early stages of irradiation and thereafter remain more or less constant at

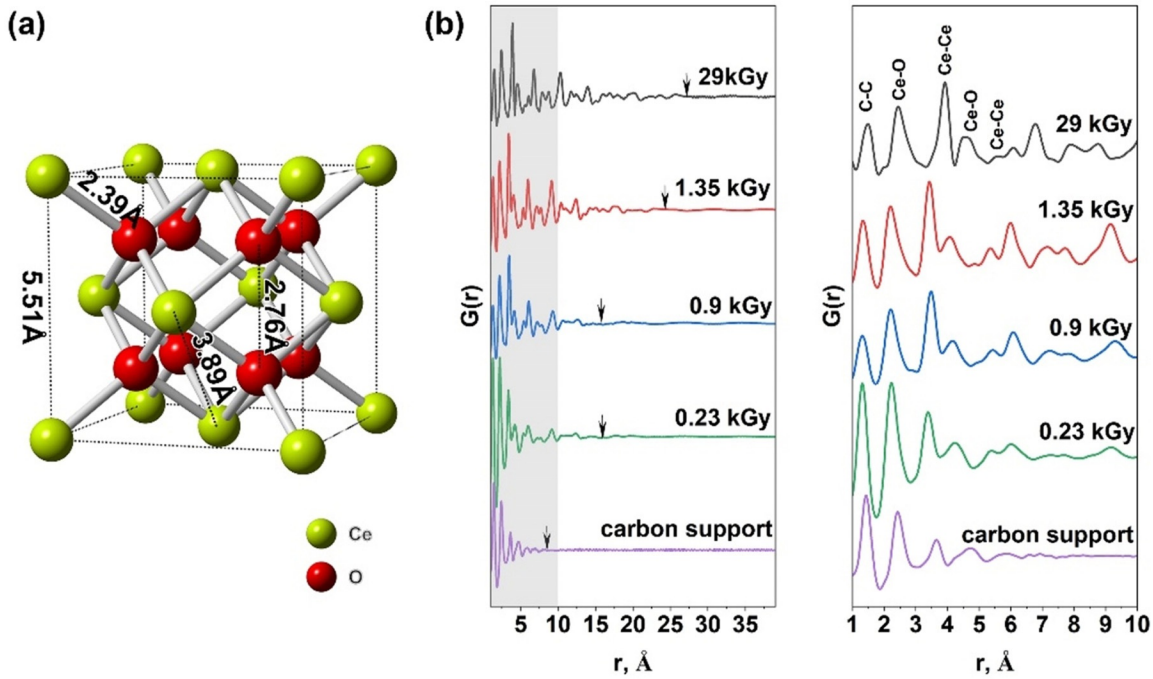

Figure 4. a) CeO_2 crystal structure ($Fm\bar{3}m$), with main distances marked. Electron radial distribution functions obtained from zero-loss energy filtered diffractions (EF-eRDFs) obtained at different doses; b) Enlargement of the EF-eRDFs in the range of 1–10 Å with main interatomic distances marked.

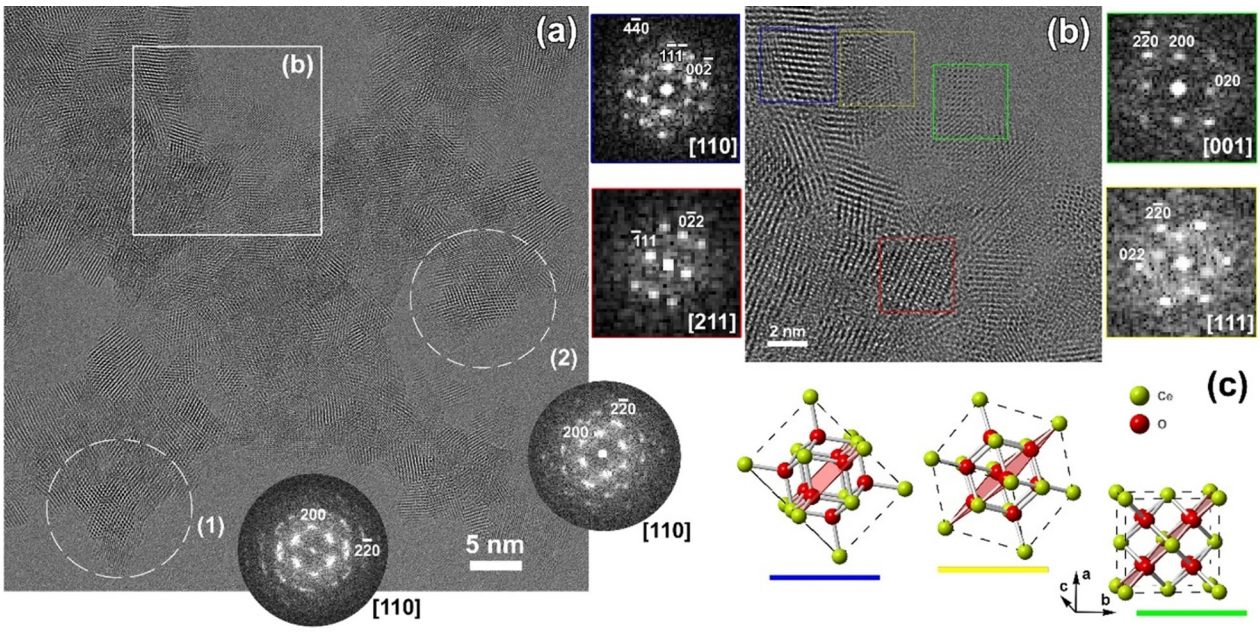

Figure 5. a) HR-TEM image of the sample obtained at 1.35 kGy. The solid line shows the area enlarged in (b). Dashed circles define areas from which FFTs (in circles) were taken. b) Enlargement from (a). Colored squares mark the areas and the corresponding FFTs. c) Crystal structure of CeO_2 showing the orientation of the individual primary particles, marked with colors on (b), with respect to each other. The (110) plane in the crystals is marked in red.

higher doses. In the present system, with continuous irradiation, the processes mentioned above will occur in parallel since Ce^{IV} is being formed continuously. In addition, the formation of mesocrystals is also occurring in parallel with the other processes. The gradual initial increase in hydroxide solubility is expected to lead to a shift in the steady-state conditions towards a higher steady-state concentration of metal hydroxide at around 3 kGy. The accumulation of hydrated Ce^{IV}-hydroxides eventually leads to the formation of large aggregates. However, with the continuous formation

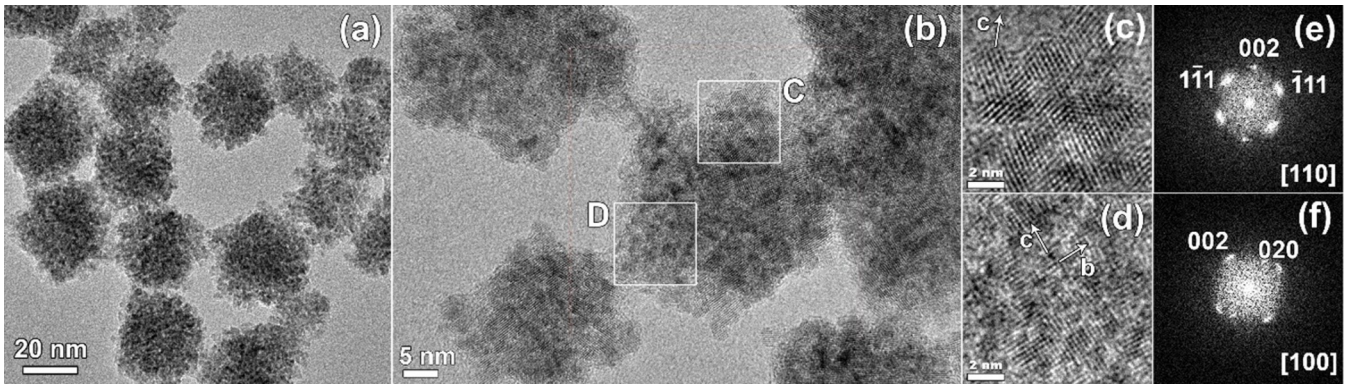

Figure 6. a,b) HR-TEM images of CeO_2 sample obtained at a total dose of 6.1 kGy; c,e) Enlargement of area C and the corresponding FFT; d,f) Enlargement of area D and the corresponding FFT. Arrows marks directions of the unit cell.

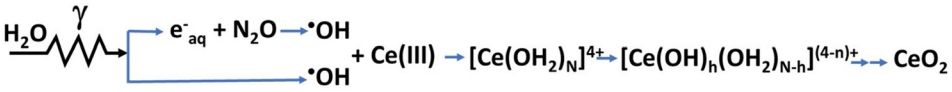

Figure 7. Basic reactions pathway for the radiation induced synthesis of CeO_2.

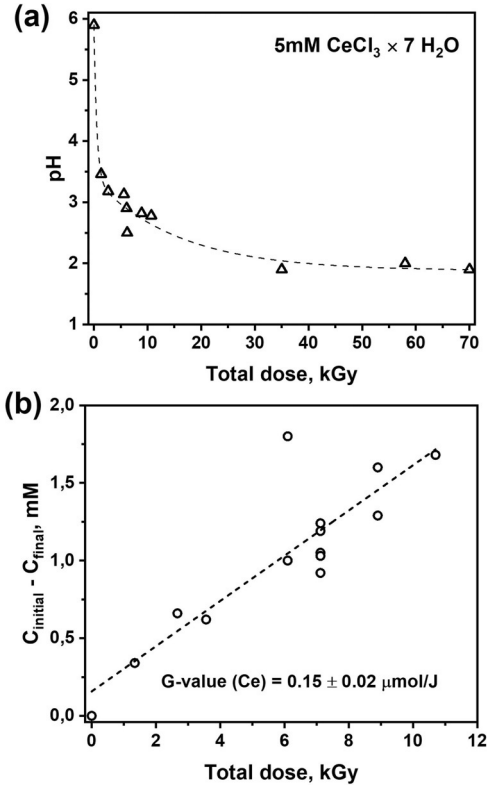

Figure 8. a) pH of precursor solutions as a function of total dose; b) Difference in Ce species concentration in solution before ($C_{initial}$) and after (C_{final}) irradiation as a function of total dose. G-value for consumption of Ce upon γ-irradiation, determined from the slope is labelled.

of Ce^{IV}-hydroxides there will be aggregates of all sizes present in the system at all times. The smaller fractions of these aggregates cannot be separated from the solution by centrifugation which can partly explain the low apparent conversion yields for Ce^{III}, shown in Figure 8(b). During TEM sample preparation, the solvent evaporates leaving CeO_2 as well as aggregates of hydrated Ce^{IV}-hydroxides on the surface.[51] The latter appear as an amorphous phase in the TEM-images.

The previously mentioned transition from loosely coordinated aggregates of primary particles to mesocrystals at around 0.45 kGy and the subsequent increase in mesocrystal size up to around 2.7 kGy may be attributed to the change in pH that could drastically affect the surface properties. As seen in Figure 8(a), the major pH-change occurs below 3 kGy. Hence, the formation and size control of mesocrystals would appear to be largely governed by pH.

As mentioned above, the cut-off distances of the EF-eRDFs of the primary particles do not appear to change after reaching a dose of 1.35 kGy. As the pH-change between 1.35 and 2.7 kGy is relatively small, the initial change in cut-off distance may also be a pH-effect. This could very well be coupled to the initially increasing steady-state concentration of metal hydroxide. It has been shown that metal oxide crystallization from solutions may occur through the formation of an intermediate hydroxide phase, and the process of oxide crystallization is attributed to a de-hydration of the hydroxides.[47] In our case, the crystallization (via possible de-hydration) is initiated by irradiation because the mesocrystal size varies with the total dose but does not depend on the residence time of particles in solution, which means that the formation of mesocrystals ends when irradiation stops.

The formed mesocrystals, when in solution, are mainly randomly oriented relative to each other. However, upon slow drying at ambient conditions, these particles start to assemble and form an ordered microscopic structure: supracrystals (Figure 9).

One can see that large (up to mm in size) ordered structures are formed. The SEM images clearly show that supracrystals consist of particles of about 27–30 nm in size, which are aligned with respect to each other. The size of nanoparticles coincides with the size of mesocrystals obtained at this dose. The FFT patterns obtained from several areas of

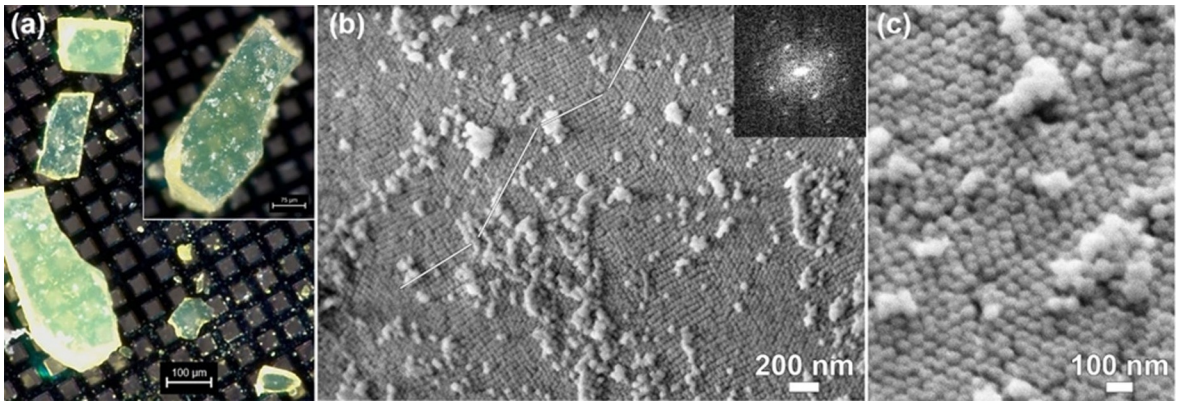

Figure 9. Supracrystals, obtained from the sample exposed to 6.14 kGy and then left to dry for several months. a) Optical image, b,c) Scanning electron microscopy (SEM) image, obtained using secondary electron detector. White lines are guidance for the eye to show different alignment of mesocrystals. Inset shows the FFT pattern obtained from the middle area of the image.

supracrystals (from the SEM images) can be described within the tetragonal unit cell. It is important to mention that these supracrystals fall apart into separate units (mesocrystals) when immersed in water and ultrasonicated for a few minutes. This indicates that while drying, adsorbed water molecules leave the surface of the particles, leading to the changes of the surface properties.[52,53] Capillary forces guide the formation of the supracrystals but no strong bonding is formed between individual mesocrystals.

The different stages of CeO_2 formation observed in the current study are schematically depicted in Figure 10. As shown in the figure, oxidation of Ce^{III} to Ce^{IV} results in Ce^{IV}-hydroxides formation. Thereafter, CeO_2 primary particle nucleation and growth followed by their self-assembly into mesocrystals, take place inside an intermediate Ce^{IV}-hydroxide phase. This intermediate phase may form continuously either until all Ce^{3+} is consumed in solution (at doses ≤ 11 kGy) or until irradiation is stopped. The composition of the intermediate is most probably variable since the dehydration of the earlier-formed and hydrolysis of the later-formed hydroxides occurs simultaneously. At the early stages of the formation of CeO_2 mesocrystals, assemblies of primary particles ("pre-mesocrystals") are found inside an amorphous phase, which suggests that this Ce^{IV}-hydroxide phase helps to guide oriented attachment by providing a constrained environment. In the particular case of the studied reaction, we found that mutual alignment of particles to mesocrystals is complex and is guided by different mechanisms,[19,54] including (i) particle alignment inside the constrained environment of the intermediate phase based on simple geometric arguments and (ii) the formation of so-called "mineral bridges".[55,56]

The mechanism proposed here is different from the mechanism for radiation-induced synthesis of metal clusters, where the formation of nanoparticles induced by radiolytic reduction of soluble metal precursor ions can often be described as Ostwald ripening.[57,58] The formation of an oxide is in general more complex than the formation of a metal, and therefore comparison to the mechanism of oxide formation is more relevant. In a recent study by Sutherland et al.,[59] the mechanism of radiation-induced formation of iron-oxide nanoparticles was investigated by using an approach similar to this work. It was found that the iron-oxide particle size at a given absorbed dose increases with increasing initial Fe^{2+} concentration. This is attributed to the adsorption of Fe^{2+} onto the solid phase primarily formed through radiolytic oxidation of Fe^{2+} to Fe^{3+} and the subsequent hydrolysis to form hydroxide. The structural investigation of iron-oxide also shows that the particle size increases

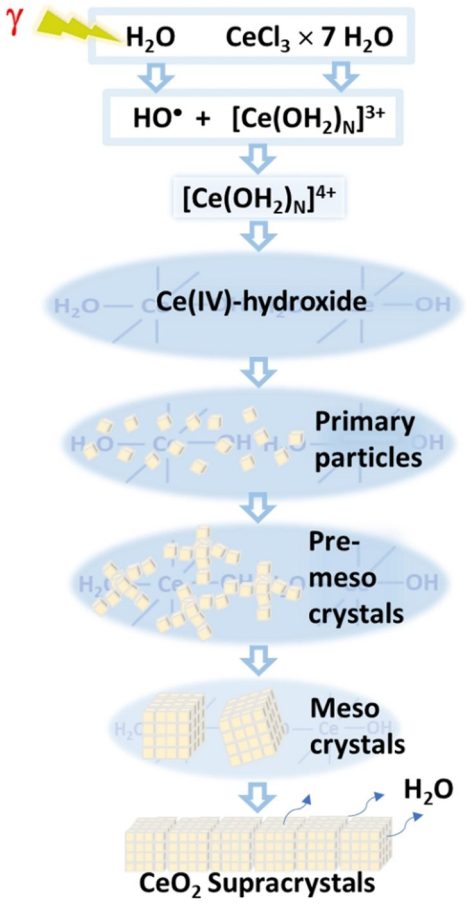

Figure 10. Schematic of CeO_2 mesocrystals formation in solution driven by γ-radiation.

with absorbed dose and the aggregation into mesocrystals does not occur. As mentioned above for the case of CeO_2, experiments using different initial Ce^{3+} concentrations do not reveal any significant differences in primary particle size as a function of initial Ce^{3+} concentration. Also, the conversion of Ce^{3+} to Ce^{4+} at a given dose does not display any dependence on initial Ce^{3+} concentration. Hence, the growth mechanism of CeO_2 primary particles does not involve adsorption of Ce^{3+} onto the Ce^{IV}-phase, in sharp contrast to what was observed for the iron-oxide. Judging from the results presented in this work and the comparison given above, we conclude that the radiation-driven step in the formation of CeO_2 mesocrystals is solely the oxidation of Ce^{3+} leading to the formation of an amorphous Ce^{IV}-hydroxide phase within which nucleation of CeO_2 primary particles and the subsequent aggregation of primary particles into mesocrystals occur without direct influence from radiolysis. The maximum primary particle size that can be achieved through this mechanism is limited by the amount of amorphous phase in each gel particle divided by the number of nuclei formed. The subsequent formation of mesocrystals seems to occur within each gel particle (i.e., not between different gel particles) which thereby limits the mesocrystal size. The fact that the primary particles as well as the mesocrystals are uniform in size implies that also the Ce^{IV}-hydroxide gel particles are uniform in size. This size could possibly be dependent on the dose rate.

Upon slow drying, CeO_2 mesocrystals form ordered supracrystals. Their formation is guided by capillary forces and provides a promising way to apply a bottom-up approach to design artificial solids or films with unique transport, optical and magnetic properties.[60,61]

It is important to mention that in many systems particle assembly requires presence of mediates[18,52] at the surface, and indeed, these mediates in the form of surfactants, polymers and complexing agents are often added to different systems.[10,13,61] Additional chemicals contribute to the complexity of the chemistry and physics of crystal growth. In our case no additives are required which allowed us to separate the sequential stages of the CeO_2 mesocrystal formation in solution. The proposed crystallization pathway might be a general route for the formation of oxide particles in aqueous reaction systems.

Conclusion

We investigate the formation of CeO_2 mesocrystals in aqueous $CeCl_3 \times 7H_2O$ solution using γ-radiation induced synthesis. Since hydroxyl radicals formed as a result of water radiolysis are the main reactive species responsible for the conversion of soluble Ce^{III} to less soluble Ce^{IV}, and no other reactants are added, the proposed reaction system can serve as an ideal model for studying the formation of mesocrystals in solutions. Our time-dependent studies of structure, morphology and composition of the obtained yellow precipitates revealed that the formation of CeO_2 mesocrystals occurs via several stages and follows a non-classical crystallization pathway. The formation of the amorphous intermediate (hydrated Ce^{IV}-hydroxides) is an important part of the process, since the nucleation of CeO_2 primary particles and their subsequent alignment into mesocrystals take place inside the intermediate hydroxide phase. The primary CeO_2 particles reach a final size of 3 nm at the early stages of the reaction (≤ 1.35 kGy), at which a rapid decrease in the pH value is observed. Mutual alignment of the primary particles into mesocrystals is guided by confinement of the amorphous intermediate phase and is accompanied by the formation of "mineral bridges". Further alignment of the obtained mesocrystals into supracrystals is possible upon slow drying.

Acknowledgements

We gratefully acknowledge financial support by the Max Planck Society. Y.Y. and I.L.S. acknowledge financial support from Swedish Foundation for Strategic Research (SSF). Z.L. acknowledges China Scholarship Council (CSC) for financial support.

Conflict of Interest

The authors declare no conflict of interest.

Keywords: CeO_2 · hierarchical architectures · mesocrystal formation · non-classical crystallization · γ-radiation-induced synthesis

[1] H. C. Yao, Y. F. Yao, *J. Catal.* **1984**, *86*, 254 – 265.
[2] T. Montini, M. Melchionna, M. Monai, P. Fornasiero, *Chem. Rev.* **2016**, *116*, 5987 – 6041.
[3] B. Li, T. Gu, T. Ming, J. Wang, P. Wang, J. Wang, J. C. Yu, *ACS Nano* **2014**, *8*, 8152 – 8162.
[4] I. Celardo, J. Z. Pedersen, E. Traversa, L. Ghibelli, *Nanoscale* **2011**, *3*, 1411 – 1420.
[5] L. A. De Faria, S. Trasatti, *J. Colloid Interface Sci.* **1994**, *167*, 352 – 357.
[6] H. Wang, J. J. Zhu, J. M. Zhu, X. H. Liao, S. Xu, T. Ding, H. Y. Chen, *Phys. Chem. Chem. Phys.* **2002**, *4*, 3794 – 3799.
[7] M. Hirano, E. Kato, *J. Am. Ceram. Soc.* **1999**, *82*, 786 – 788.
[8] P. Chen, I. Chen, *J. Am. Ceram. Soc.* **1993**, *76*, 1577 – 1583.
[9] W. P. Hsu, R. L. Önnquist, E. Matijevic, *Langmuir* **1988**, *4*, 31 – 37.
[10] N. Krishna Chandar, R. Jayavel, *Appl. Nanosci.* **2013**, *3*, 263 – 269.
[11] W. Deng, X. Wang, F. Jiao, K. Zhu, *J. Nanopart. Res.* **2013**, *15*, 1944.
[12] J. Calvache-Muñoz, F. A. Prado, J. E. Rodríguez-Páez, *Colloids Surf. A* **2017**, *529*, 146 – 159.
[13] S. Yang, L. Gao, *J. Am. Chem. Soc.* **2006**, *128*, 9330 – 9331.
[14] A. A. Litwinowicz, S. Takami, S. Asahina, X. Hao, A. Yoko, G. Seong, T. Tomai, T. Adschiri, *CrystEngComm* **2019**, *21*, 3836 – 3843.
[15] X. Lu, X. Li, F. Chen, C. Ni, Z. Chen, *J. Alloys Compd.* **2009**, *476*, 958 – 962.
[16] B. Xue, R. Liu, Z. De Xu, *Mater. Sci. Eng. B* **2011**, *176*, 210 – 216.
[17] D. Wang, Y. Kang, V. Doan-Nguyen, J. Chen, R. Küngas, N. L. Wieder, K. Bakhmutsky, R. J. Gorte, C. B. Murray, *Angew. Chem. Int. Ed.* **2011**, *50*, 4378 – 4381; *Angew. Chem.* **2011**, *123*, 4470 – 4473.

[18] H. Cölfen, M. Antonietti, *Angew. Chem. Int. Ed.* **2005**, *44*, 5576 – 5591; *Angew. Chem.* **2005**, *117*, 5714 – 5730.
[19] H. Cölfen, S. Mann, *Angew. Chem. Int. Ed.* **2003**, *42*, 2350 – 2365; *Angew. Chem.* **2003**, *115*, 2452 – 2468.
[20] H. Cölfen, M. Antonietti, *Mesocrystals and Nonclassical Crystallization*, Wiley, Hoboken, **2008**.
[21] D. Gebauer, H. Cölfen, *Nano Today* **2011**, *6*, 564 – 584.
[22] I. L. Soroka, K. K. Norrfors, N. V. Tarakina, *Cryst. Growth Des.* **2019**, *19*, 5275 – 5282.
[23] V. K. LaMer, R. H. Dinegar, *J. Am. Chem. Soc.* **1950**, *72*, 4847 – 4854.
[24] W. K. Burton, N. Cabrera, F. C. Frank, *Philos. Trans. R. Soc. A* **1951**, *243*, 299 – 358.
[25] C. Dispenza, N. Grimaldi, M. A. Sabatino, I. L. Soroka, M. Jonsson, *J. Nanosci. Nanotechnol.* **2015**, *15*, 3445 – 3467.
[26] J. Belloni, M. Mostafavi, *Radiation Chemistry: Present Status and Future Trends* (Eds.: C. D. Jonah, B. C. M Rao), Elsevier, Amsterdam, **2001**.
[27] H. Remita, S. Remita, *Recent trends in Radiation Chemistry*, World Scientific Publishing Co., Singapore, Ch. 13, pp. 347 – 383, **2010**.
[28] M. Kelm, J. Lilie, A. Henglein, *J. Chem. Soc. Faraday Trans. 1* **1975**, *71*, 1132 – 1142.
[29] B. G. Ershov, E. Janata, A. Henglein, *J. Phys. Chem.* **1994**, *98*, 7619 – 7623.
[30] M. Treguer, C. de Cointet, H. Remita, J. Khatouri, M. Mostafavi, J. Amblard, J. Belloni, *J. Phys. Chem. B* **1998**, *102*, 4310 – 4321.
[31] J. L. Marignier, J. Belloni, M. O. Delcourt, J. P. Chevalier, *Nature* **1985**, *317*, 344 – 345.
[32] P. A. Yakabuskie, J. M. Joseph, P. Keech, G. A. Botton, D. Guzonas, J. C. Wren, *Phys. Chem. Chem. Phys.* **2011**, *13*, 7198 – 7206.
[33] L. M. Alrehaily, J. M. Joseph, M. C. Biesinger, D. A. Guzonas, D. A. J. C. Wren, *Phys. Chem. Chem. Phys.* **2013**, *15*, 1014 – 1024.
[34] P. Yadav, R. T. Olsson, M. Jonsson, *Radiat. Phys. Chem.* **2009**, *78*, 939 – 944.
[35] Z. Li, Y. Yang, A. Relefors, X. Y. Kong, G. M. Siso, B. Wickman, Y. Kiros, I. L. Soroka, *J. Colloid Interface Sci.* **2021**, *583*, 71 – 79.
[36] J. W. T. Spinks, R. J. Woods, *An Introduction to Radiation Chemistry*, Wiley, New York, **1990**.
[37] P. A. Yakabuskie, J. M. Joseph, C. R. Stuart, J. C. Wren, *J. Phys. Chem. A* **2011**, *115*, 4270 – 4278.
[38] G. V. Buxton, C. L. Greenstock, W. P. Helman, A. B. Ross, *J. Phys. Chem. Ref. Data* **1988**, *17*, 513 – 886.
[39] M. V. Vladimirova, A. S. Milovanova, *High Energy Chem.* **1975**, *9*, 309 – 311.
[40] M. WoŁcyrz, L. Kepinski, *J. Solid State Chem.* **1992**, *99*, 409 – 413; M. G. Harwood, *Nature* **1949**, *164*, 787.
[41] L. Chen, P. Fleming, V. Morris, J. D. Holmes, M. A. Morris, *J. Phys. Chem. C* **2010**, *114*, 12909 – 12919.
[42] R. K. Hailstone, A. G. DiFrancesco, J. G. Leong, T. D. Allston, K. J. Reed, *J. Phys. Chem. C* **2009**, *113*, 15155 – 15159.
[43] S. Tsunekawa, R. Sahara, Y. Kawazoe, K. Ishikawa, *Appl. Surf. Sci.* **1999**, *152*, 53 – 56.
[44] P. M. Diehm, P. Ágoston, K. Albe, *ChemPhysChem* **2012**, *13*, 2443 – 2454.
[45] E. V. Sturm (née Rosseeva), H. Cölfen, *Chem. Soc. Rev.* **2016**, *45*, 5821 – 5833.
[46] M. S. A. Asghar, B. J. Inkson, G. Möbus, *J. Mater. Sci.* **2020**, *55*, 2815 – 2825.
[47] A. C. Pierre, in *Introd. to Sol-Gel Process.*, Springer Nature Switzerland AG, **1998**, pp. 165 – 208.
[48] S. A. Hayes, P. Yu, T. J. O'Keefe, M. J. O'Keefe, J. O. Stoffer, *J. Electrochem. Soc.* **2002**, *149*, C623 – C630.
[49] M. F. Holovko, *Condens. Matter Phys.* **1997**, 13 – 25.
[50] T. V. Plakhova, A. Y. Romanchuk, S. N. Yakunin, T. Dumas, S. Demir, S. Wang, S. G. Minasian, D. K. Shuh, T. Tyliszczak, A. A. Shiryaev, A. V. Egorov, V. K. Ivanov, S. N. Kalmykov, *J. Phys. Chem. C* **2016**, *120*, 22615 – 22626.
[51] T. V. Plakhova, A. Y. Romanchuk, S. M. Butorin, A. D. Konyukhova, A. V. Egorov, A. A. Shiryaev, A. E. Barinchikov, P. V. Dorovatovskii, T. Huthwelker, E. Gerberg, S. Bautersg, M. M. Sozarukova, A. C. Scheinost, V. K. Ivanov, S. N. Kalmykov, K. O. Kvashnina, *Nanoscale* **2019**, *11*, 18142 – 18149.
[52] A. Corma, P. Atienzar, H. García, J. Y. Chane-Ching, *Nat. Mater.* **2004**, *3*, 394 – 397.
[53] Z.-P. Lv, M. Kapuscinski, L. Bergström, *Nat. Commun.* **2019**, *10*, 4228.
[54] K. Inumaru, *Catal. Surv. Asia* **2006**, *10*, 151 – 160.
[55] Y. Oaki, A. Kotachi, T. Miura, H. Imai, *Adv. Funct. Mater.* **2006**, *16*, 1633 – 1639.
[56] T. E. Schäffer, C. Ionescu-Zanetti, R. Proksch, M. Fritz, D. A. Walters, N. Almqvist, C. M. Zaremba, A. M. Belcher, B. L. Smith, G. D. Stucky, D. E. Morse, P. K. Hansma, *Chem. Mater.* **1997**, *9*, 1731 – 1740.
[57] A. Henglein, *Chem. Rev.* **1989**, *89*, 1861 – 1873.
[58] S. M. Ghoreishian, S. M. Kang, G. S. R. Raju, M. Norouzi, S. C. Jang, H. J. Yun, S. T. Lim, Y. K. Han, C. Roh, Y. S. Huh, *Chem. Eng. J.* **2019**, *360*, 1390 – 1406.
[59] T. I. Sutherland, C. J. Sparks, J. M. Joseph, Z. Wang, G. Whitaker, T. K. Sham, C. Wren, *Phys. Chem. Chem. Phys.* **2017**, *19*, 695 – 708.
[60] Z. Yang, J. Wei, P. Bonville, M. P. Pileni, *Adv. Funct. Mater.* **2015**, *25*, 4908 – 4915.
[61] M. P. Pileni, *C. R. Chim.* **2003**, *6*, 965 – 978.
[62] M. Wang, A. C. Leff, Y. Li, T. J. Woehl, *ACS Nano* **2021**, *15*, 2578 – 2588.

Manuscript received: September 8, 2021
Accepted manuscript online: December 3, 2021
Version of record online: December 21, 2021